

Data Efficient Lithography Modeling with Transfer Learning and Active Data Selection

Yibo Lin *Student Member, IEEE*, Meng Li *Student Member, IEEE*, Yuki Watanabe, Taiki Kimura, Tetsuaki Matsunawa, Shigeki Nojima, David Z. Pan *Fellow, IEEE*

Abstract—Lithography simulation is one of the key steps in physical verification, enabled by the substantial optical and resist models. A resist model bridges the aerial image simulation to printed patterns. While the effectiveness of learning-based solutions for resist modeling has been demonstrated, they are considerably data-demanding. Meanwhile, a set of manufactured data for a specific lithography configuration is only valid for the training of one single model, indicating low data efficiency. Due to the complexity of the manufacturing process, obtaining enough data for acceptable accuracy becomes very expensive in terms of both time and cost, especially during the evolution of technology generations when the design space is intensively explored. In this work, we propose a new resist modeling framework for contact layers, utilizing existing data from old technology nodes and active selection of data in a target technology node, to reduce the amount of data required from the target lithography configuration. Our framework based on transfer learning and active learning techniques is effective within a competitive range of accuracy, i.e., 3-10X reduction on the amount of training data with comparable accuracy to the state-of-the-art learning approach.

Index Terms—Lithography modeling, Machine learning, Transfer learning, Active learning, Convolutional neural networks, Residual neural networks

I. INTRODUCTION

Due to the continuous semiconductor scaling from 10nm technology node (N10) to 7nm node (N7) [1], [2], the prediction of printed pattern sizes is becoming increasingly difficult and complicated due to the complexity of manufacturing process and variations. However, complex designs demand accurate simulations to guarantee functionality and yield. Resist modeling, as a key component in lithography simulation, is critical to bridge the aerial image simulation to manufactured wafer data. Rigorous simulations that perform physics-level modeling suffer from large computational overhead, which are not suitable when used extensively. Thus compact resist models are widely used in practice.

Figure 1(a) shows the process of lithography simulations where the aerial image is computed from the input mask patterns and the optical model, and the output pattern is computed from the aerial image and the resist model. As the aerial image contains the light intensity map, the resist model needs to determine the slicing thresholds for the output patterns as shown in Figure 1(b). With the thresholds, the critical dimensions (CDs) of printed patterns can be computed, which need to match CDs measured from manufactured patterns. In practice, various factors may impact a resist model such as the physical properties of photoresist, design rules of patterns, process variations. Critical dimension usually refers to the smallest dimension on a lithography level that must be accurately controlled when fabricating a device. Here critical dimensions refer to the sizes of printed patterns.

Accurate lithography simulation like rigorous physics-based simulation is notorious for its long computational time, while simulation with compact models suffers from accuracy issues [3], [4]. On the

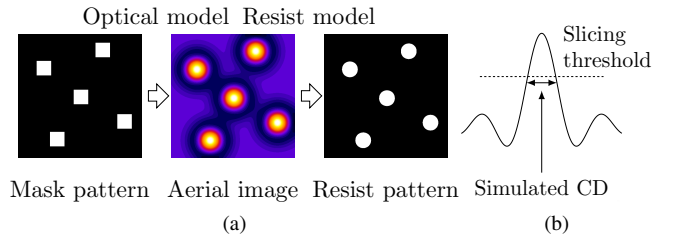


Fig. 1: (a) Process of lithography simulation with optical and resist models. (b) Thresholds for aerial image determine simulated CD, which should match manufactured CD.

other hand, machine learning techniques are able to construct accurate models and then make efficient predictions. These approaches first take training data to calibrate a model and then use this model to make predictions on testing data for validation. The effectiveness of learning-based solutions has been studied in various lithography related areas including aerial image simulation [5], hotspot detection [6]–[11], optical proximity correction (OPC) [12]–[15], sub-resolution assist features (SRAF) [16], [17], resist modeling [3], [4], etc. In resist modeling, a convolutional neural network (CNN) that predicts slicing thresholds in aerial images is proposed [4]. The neural network consists of three convolution layers and two fully connected layers. Since the slicing threshold is a continuous value, learning a resist model is a regression task rather than a classification task. Around 70% improvement in accuracy is reported compared with calibrated compact models from Mentor Calibre [18]. Shim et al. [3] propose an artificial neural network (ANN) with five hidden layers to predict the height of resist after exposure. Significant speedup is reported with high accuracy compared with a rigorous simulation.

Although the learning-based approaches are able to achieve high accuracy, they are generally data-demanding in model training. In other words, big data is assumed to guarantee accuracy and generality. Furthermore, one data sample can only be used to train the corresponding model under the same lithography configuration, indicating a low data efficiency. Here data efficiency evaluates the accuracy a model can achieve given a specific amount of data, or the amount of data samples are required to achieve target accuracy. Nevertheless, obtaining a large amount of data is often expensive and time-consuming, especially when the technology node switches from one to another and the design space is under active exploration, e.g., from N10 to N7. The lithography configurations including optical sources, resist materials, etc., are frequently changed for experiments. Therefore, a fast preparation of models with high accuracy is urgently desired. In addition, it remains to be a question that what are the best designs for building a model. Typical practice of regular array patterns or random patterns may not be representative enough to calibrate accurate and generic models. Thus effective techniques to recognize representative designs will also be beneficial to improving data efficiency.

Y. Lin, M. Li and D. Z. Pan are with The Department of Electrical and Computer Engineering, The University of Texas at Austin, TX, USA.

Y. Watanabe, T. Kimura, T. Matsunawa, and S. Nojima are with Toshiba Memory Corporation, Yokohama, Japan.

Different from previous approaches, in this work, we assume the availability of large amounts of data from the previous technology generation with old lithography configurations and small amounts of data from a target lithography configuration. We focus on increasing the data efficiency by 1) reusing those from other lithography configurations and transfer the knowledge between different configurations; 2) active selection of data samples in the target configuration, also known as active learning. The objective is to achieve accurate resist models with significantly fewer data to a target configuration. The major contributions are summarized as follows.

- We propose a high performance resist modeling technique based on the residual neural network (ResNet).
- We propose a transfer learning scheme for ResNet that can reduce the amount of data with a target accuracy by utilizing the data from other configurations.
- We propose an active learning scheme based on K-Medoids algorithm with theoretical insights for both CNN and ResNet.
- The experimental results demonstrate 3-10X reduction in the amount of training data to achieve accuracy comparable to the state-of-the-art learning approach [4].

The rest of the paper is organized as follows. Section II illustrates the problem formulation. Section III explains the details of our approach. The effectiveness of our approach is verified in Section IV and the conclusion is drawn in Section V.

II. PRELIMINARIES

In this section, we will briefly introduce the background knowledge on lithography simulation and resist modeling. Then the problem formulation is explained. We mainly focus on contact layers in this work, but our methodology shall be applicable to other layers. For simplicity, we use the word *label* to represent the target value for prediction, e.g., threshold, given a data sample; we also use the phrase *unlabelled* data to denote data samples whose labels are unknown.

A. Lithography Simulation

Lithography simulation is generally composed of two stages, i.e., optical simulation and resist simulation, where optical and resist models are required, respectively. In the optical simulation, an optical model, characterized by the illumination tool, takes mask patterns to compute aerial images, i.e., light intensity maps. Then in the resist simulation, a resist model finalizes the resist patterns with the aerial images from the optical simulation. Generally, there are two types of resist models. One is a variable threshold resist (VTR) model in which the thresholds vary according to aerial images, and the other is a constant threshold resist (CTR) model in which the light intensity is modulated in an aerial image. We adopt the former since it is suitable to learning-based approaches [4].

Figure 2 shows an example of lithography simulation for a clip with three contacts. We assume that proper resolution enhancement techniques (RETs) such as OPC and SRAF have been applied before the computation of the aerial image [19]. The optical simulation generates the aerial image, as shown in Figure 2(b). Resist simulation then computes the thresholds in the aerial image to predict printed patterns. If we want to measure the widths of contacts along the dotted line in Figure 2(c), the light intensity profiling can be extracted from the aerial image along the line and calculates the CDs for each contact with the thresholds.

B. Historical Data and Transfer Learning

Since the lithography configurations evolve from one generation to another with the advancement of technology nodes, there are plenty

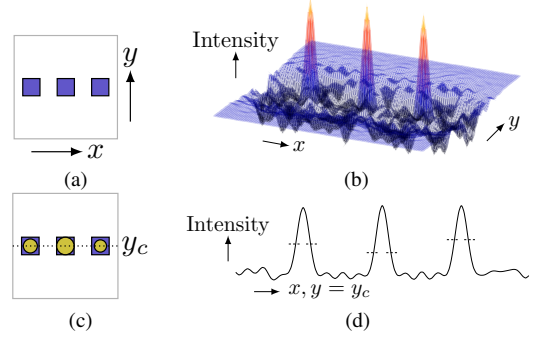


Fig. 2: (a) Design target of 3 contacts and (b) the light intensity plot of aerial image. Assume that RETs such as SRAF and OPC have been already applied to the contacts before optical simulation. (c) A dotted line horizontally crosses the centers at $y = y_c$ and the circles denote the contours of printed patterns. (d) Light intensity profiling along the dotted line at $y = y_c$ extracted from the aerial image and different slicing thresholds for each contact.

TABLE I: Lithography Configurations for N10 and N7

	N10	N7	
		N7 _a	N7 _b
Design Rule	A	B	B
Optical Source	A	B	B
Resist Material	A	A	B

of historical data available for the old generation. As mentioned in Section I, accurate models require a large amount of data for training or calibration, which are expensive to obtain during the exploration of a new generation. If the lithography configurations have no fundamental changes, the knowledge learned from the historical data may still be applicable to the new configuration, which can eventually help to reduce the amount of new data required.

Transfer learning represents a set of techniques to transfer the knowledge from one or multiple source domains to a target domain, utilizing the underlying similarity between the data from these domains. Various studies have explored the effectiveness of knowledge transfer in image recognition and robotics [20]–[22], while it is not clear whether the knowledge between different resist models is transferable or not.

In this work, we consider the evolution of the contact layer from the cutting edge technology node N10 to N7 [1], [2]. A large amount of available N10 data are assumed. During the evolution to N7, different design rules for mask patterns, optical sources and resist materials for lithography are explored. Table I shows the lithography configurations considered for N10 and N7. Differences in letters *A*, *B* represent different configurations of design rules, optical sources, or resist materials. One configuration for N10 is considered, while two configurations are considered for N7, i.e., N7_a, N7_b, with two kinds of resist materials (about 20% difference in the slopes of dissolution curves). From N10 to N7, both the design rules and optical sources are changed. For N10, we consider a pitch of 64nm with double patterning lithography, while for N7, the pitch is set to 45nm with triple patterning lithography [1]. The width of each contact is set to half pitch. The lithography target of each contact is set to 60nm for both N10 and N7. Optical sources calibrated with industrial strength for N10 and N7 are shown in Figure 3, with the same type of illumination shapes.

Various combinations of knowledge transfer can be explored from Table I, such as N10→N7, N7_i→N7_j, and N10+N7_i→N7_j, where $i \neq j$, $i, j \in \{a, b\}$.

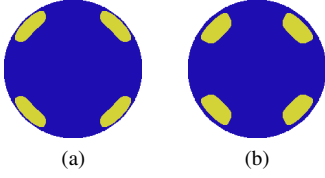


Fig. 3: Optical sources (yellow) for (a) N10 and (b) N7.

C. Active Learning for Regression

Active learning assumes unlabelled data samples exist in a pool or can be generated. Querying for data labels is very expensive and the amount of queries should be minimized. Thus selecting the proper and limited portion of data samples for querying is essential to modeling accuracy.

We define the problem of pool-based active learning as: given a pool of unlabelled data samples, select k samples to query for labels and train a model to maximize the accuracy across the entire dataset. Be aware that the selection of data samples should not depend on data labels since labels are unknown before querying. Hence, active learning is very effective in improving data efficiency without the requirement of any additional labelled data.

There are extensive studies for active learning in classification for CNN and SVM [23]–[26]. A few studies have explored active learning for support vector regression (SVR) and multi-layer perception (MLP) [27], [28]. Most techniques are categorized into confidence level or clustering approaches. Confidence level approaches tend to choose data samples with low prediction confidence, and clustering approaches choose representative subset of data samples among an entire dataset. There are also successful applications of active learning in VLSI CAD related areas [29]–[31].

However, practical studies on active learning techniques for regression tasks with CNN or ResNet are lacking, and its performance when combined with transfer learning is unclear. It is often difficult to evaluate the confidence level with large and complicated models like CNN or ResNet, while clustering approaches only rely on the general properties of data samples and models. Therefore, we explore effective clustering strategies for active selection of data samples, which are suitable to regression tasks with CNN and ResNet.

D. Learning-based Resist Modeling

The thresholds of positions near the contacts are of significant importance since they usually determine the boundaries of printed contacts. Hence we consider the middle of the left, right, bottom and top edges for each contact, as shown in Figure 4(a), where the positions for prediction are highlighted with black dots. As the threshold is mainly influenced by the surrounding mask patterns, resist models typically compute the threshold using a clip of mask patterns centered by a target position. To measure the thresholds in Figure 4(a), we select a clip where the target position lies in its center, as shown in Figure 4(b) to Figure 4(e). The task of a resist model is to compute the thresholds for these positions of each contact [4].

Learning-based resist modeling consists of two phases, i.e., training and testing. In the training phase, training dataset with both aerial images and thresholds are used to calibrate the model, while in the testing phase, the model predicts thresholds for the aerial images from the testing dataset.

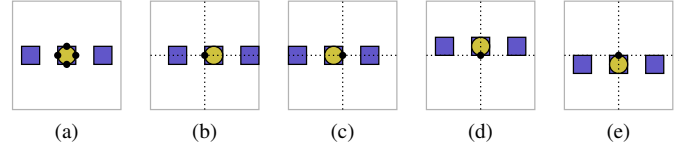


Fig. 4: (a) The thresholds for the middle of the 4 edges of the center contact are predicted. (b) (c) (d) (e) The clip window is shifted such that the target position lies in the center of the clip.

E. Problem Formulation

The accuracy¹ of a model is evaluated with root mean square (RMS) error defined as follows,

$$\epsilon = \sqrt{\frac{1}{N} \sum_{i=1}^N (\hat{y} - y)^2}, \quad (1)$$

where N denotes the amount of samples, y denotes the golden values and \hat{y} denotes the predicted values. We further define relative RMS error,

$$\epsilon_r = \sqrt{\frac{1}{N} \sum_{i=1}^N \left(\frac{\hat{y} - y}{y} \right)^2}, \quad (2)$$

where a relative ratio of error from the golden values can be represented. Both metrics can refer to errors in either CD or threshold. Although during model training, the RMS error of threshold is generally minimized due to easier computation, the eventual model is often evaluated with the RMS error of CD for its physical meaning to the patterns. The RMS errors in threshold and CD essentially have almost the same fidelity, and usually yield consistent comparison. For convenience, we report relative RMS error in threshold (ϵ_r^{th}) for comparison of different models since it removes the dependency to the scale of thresholds, and use RMS error in CD (ϵ^{CD}) for data efficiency related comparison.

Definition II.1 (Data Efficiency). *The amount of target domain data required to learn a model with a given accuracy.*

Given a specific amount of data from a target domain, if one can learn a model with a higher accuracy than another, it also indicates higher data efficiency. Thus improving model accuracy benefits data efficiency as well.

The resist modeling problem is defined as follows.

Problem II.2 (Learning-based Resist Modeling). *Given a dataset containing information of aerial images and thresholds at their centers, train a resist model that can maximize the accuracy for the prediction of thresholds.*

In practice, accuracy is not the only objective. The amount of training data should be minimized as well due to the high cost of data preparation. Therefore, we propose the problem of data efficient resist modeling as follows.

Problem II.3 (Data Efficient Resist Modeling). *Given a labelled N10 dataset containing aerial images and thresholds, and an unlabelled N7 dataset containing aerial images only, train a resist model for target dataset $N7_i$ that can achieve high accuracy and meanwhile query labels for as few $N7_i$ data samples as possible, where $i \in \{a, b\}$.*

Minimizing the times of label querying is equivalent to minimizing the cost of data preparation, since the most expensive part is to

¹Note that the accuracy we talk about in this paper refers to the accuracy at end of lithography flow including all RETs.

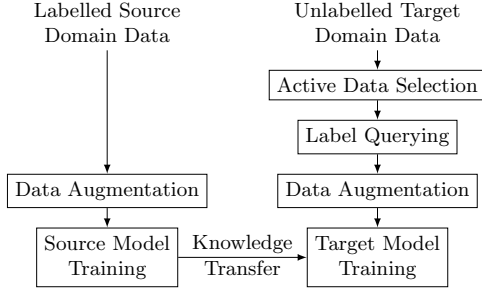


Fig. 5: Training flow with transfer learning and active learning.

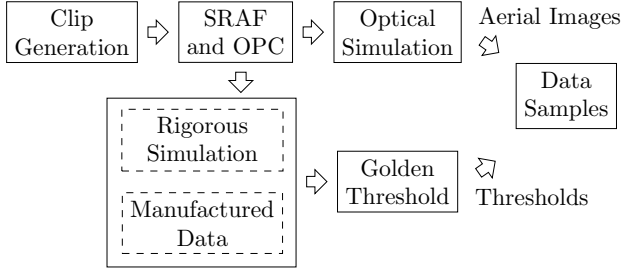


Fig. 6: Flow of data preparation.

obtain the labels, i.e., thresholds, through either manufactured wafer data or rigorous simulation.

III. ALGORITHMS

In this section, we will explain the structure of our models and then the details regarding the transfer learning and active learning schemes. Figure 5 shows the overall training flow. We first leverage labelled source domain data to train a source domain model. Then before training the target domain model, active learning is applied for active selection of data samples for label querying. The target domain model is eventually trained with selected data samples and knowledge transferred from the source domain model. Data augmentation in Section III-A2 is applied before training of both source and target models.

A. Data Preparation

Figure 6 gives the flow of data preparation. We first generate clips and perform SRAF insertion and OPC. The aerial images are then computed from the optical simulation, and at the same time, the golden thresholds need to be computed from either the rigorous simulation or the manufactured data. Each data sample consists of an aerial image and the threshold at its center.

1) *Clip Generation*: Following the design rules such as minimum pitch of contacts, we generate three types of $2 \times 2 \mu\text{m}$ clips. It is necessary to ensure that there is a contact in the center of each clip since that is the target contact for threshold computation.

Contact Array. All possible $m \times n$ arrays of contacts within the dimensions of clips are enumerated. The steps of the arrays can be multiple times of the minimum pitch p , i.e., $p, 2p, 3p, \dots$, in horizontal or vertical directions. An example of 3×3 contact array with a certain pitch is shown in Figure 7(a). It needs to mention that the same 3×3 contact array with different steps should be regarded as different clips due to discrepant spacing.

Randomized Contact Array. The aforementioned contact arrays essentially distribute contacts on grids and fill all the slots in the grid maps. The randomization of contact arrays is implemented by a random distribution of contacts in those grid maps. Figure 7(b)

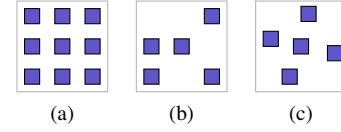


Fig. 7: (a) A clip of 3×3 contact array. (b) A clip of 3×3 randomized contact array. (c) A clip of contacts with random positions.

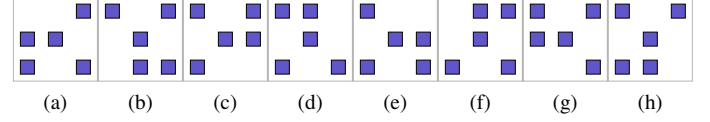


Fig. 8: Combinations of rotation and flipping. (a) Original. (b) Rotate 90° . (c) Rotate 180° . (d) Rotate 270° . (e) Flip. (f) Flip and rotate 90° . (g) Flip and rotate 180° . (h) Flip and rotate 270° .

shows an example of randomized contact array from the 3×3 contact array in Figure 7(a). Various distribution of contacts can be generated even from the same grid maps.

Contacts with Random Positions. Contacts in this type of clips do not necessarily align to any grid map, as their positions are randomly generated, while the design rules are still guaranteed. An example is shown in Figure 7(c). No matter how the surrounding contacts change, the contact in the center of the clip should remain the same.

2) *Data Augmentation*: Due to the symmetry of optical sources in Figure 3, data can be augmented with rotation and flipping, improving the data efficiency [32]. Eight combinations of rotation and flipping are shown in Figure 8, where new data samples are obtained without new thresholds. Data augmentation inflates datasets to obtain models with better generalization.

B. Convolutional Neural Networks

Convolutional neural networks (CNN) have demonstrated impressive performance on mask related applications in lithography such as hotspot detection, and resist modeling [4], [9]. The structure of CNN mainly includes convolution layers and fully connected layers. Features are extracted from convolution layers and then classification or regression is performed by fully connected layers. Figure 11(a) illustrates a CNN structure with three convolution layers and two fully connected layers [4]. The first convolution layer has 64 filters with dimensions of 7×7 . Although not explicitly shown most of the time, a rectified linear unit (ReLU) layer for activation is applied immediately after the convolution layer, where the ReLU function is defined as,

$$f(x^{l-1}) = \begin{cases} x^{l-1}, & \text{if } x^{l-1} \geq 0, \\ 0, & \text{otherwise.} \end{cases} \quad (3)$$

Then the max-pooling layer performs down-sampling with a factor of 2 to reduce the feature dimensions and improve the invariance to translation [32]. After three convolution layers, two fully connected layers are applied where the first one has 256 hidden units followed with a ReLU layer and a 50% dropout layer, and second one connects to the output.

C. Residual Neural Networks

One way to improve the performance of CNN is to increase the depth for a larger capacity of the neural networks. However, the counterintuitive degradation of training accuracy in CNN is observed when stacking more layers, preventing the neural networks from

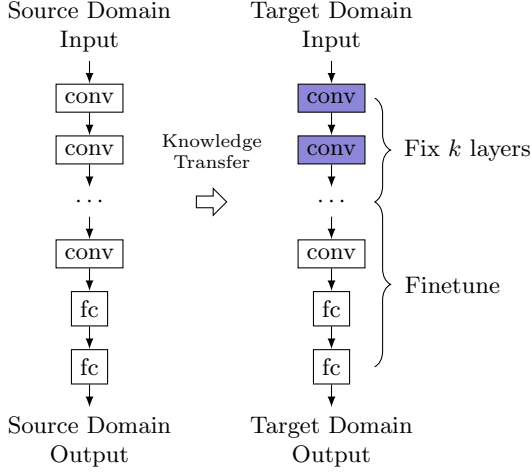


Fig. 12: Transfer learning scheme with the first k layers fixed when training for target domain, denoted as TF_k .

normalization. In other words, raw aerial images are fed to the neural networks. The benefits of scaling and normalization are left to future work.

E. Active Learning with Clustering

Although transfer learning is potentially able to improve the accuracy of the target dataset using knowledge from a source dataset, selection of representative target data samples may further improve the accuracy. Let D be the unlabeled dataset in the target domain and s be the set of selected data samples for label querying, where $|s| \leq k$ and k is the maximum number of data samples for querying. For any $(\mathbf{x}_i, y_i) \in D$, \mathbf{x}_i is the feature, e.g., aerial image, and y_i is the label, e.g., threshold, where y_i is unknown for D . Consider a loss function $l(\mathbf{x}_i, y_i; \mathbf{w})$ parameterized over the hypothesis class (\mathbf{w}) , e.g., parameters of a learning algorithm. The objective of active learning is to minimize the average loss of dataset D with a model trained from s ,

$$\min_{s: |s| \leq k, s \in D} \frac{1}{n} \sum_{i=1}^n l(\mathbf{x}_i, y_i; \mathbf{w}_s), \quad (4)$$

where $n = |D|$, and \mathbf{w}_s represents the parameters of a model trained from s .

We present an upper bound of Eq. (4) for any Lipschitz loss function and Lipschitz estimator. Then we show that both CNN and ResNet with non-linear ReLU activations are actually Lipschitz continuous. We also assume the training loss can drop to zero, which is likely to be achieved with large enough models.

Definition III.1. Let $g(\cdot; \cdot) : \mathbb{R}^d \times \mathbb{R}^d \rightarrow \mathbb{R}$, we say g is L_1 -Lipschitz continuous with respect to $g(\cdot; \cdot)$ if

$$|g(\mathbf{x}; \mathbf{w}) - g(\mathbf{x}'; \mathbf{w})| \leq L_1 \cdot \|\mathbf{x} - \mathbf{x}'\|.$$

We also write $g(\mathbf{x}; \mathbf{w})$ as $g_{\mathbf{w}}(\mathbf{x})$. We use Frobenius norm for norm of a matrix here, i.e., $\|\cdot\|$.

Definition III.2. Let $f(\cdot, \cdot; \cdot) : \mathbb{R}^{d_1} \times \mathbb{R} \times \mathbb{R}^{d_2} \rightarrow \mathbb{R}_{\geq 0}$, we say f is L_2 -Lipschitz continuous with respect to $f(\cdot, \cdot; \cdot)$ if

$$|f(\mathbf{x}, y; \mathbf{w}) - f(\mathbf{x}', y'; \mathbf{w})| \leq L_2 \cdot (\|\mathbf{x} - \mathbf{x}'\| + |y - y'|), \\ \forall \mathbf{x} \in \mathbb{R}^{d_1}, \forall y, y' \in \mathbb{R}, \forall \mathbf{w} \in \mathbb{R}^{d_2}.$$

We also write $f(\mathbf{x}, y; \mathbf{w})$ as $f_{\mathbf{w}}(\mathbf{x}, y)$.

We state the following theorem:

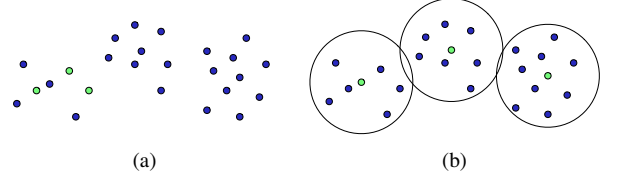


Fig. 13: Example of (a) bad data selection and (b) K-Medoids clustering selection in 2D space. Three selected points are highlighted. Circles denote three clusters centered by selected points.

Theorem III.3. Given n independent and identically distributed (i.i.d.) random samples as $D = \{\mathbf{x}_i, y_i\}_{i \in \{1, 2, \dots, n\}}$, and a set of selected points s . If the following properties hold,

- 1) loss function $l(\mathbf{x}, y; \mathbf{w})$ is λ^l -Lipschitz continuous w.r.t (\mathbf{x}, y) ;
- 2) the ground truth of label $y = f(\mathbf{x}) + \epsilon$ has the property that $f(\cdot)$ is λ^f -Lipschitz continuous and random noise $\epsilon \sim \mathcal{N}(0, \sigma^2)$;
- 3) $\hat{f}(\cdot)$ in the prediction function $\hat{y} = \hat{f}(\mathbf{x})$ is $\lambda^{\hat{f}}$ -Lipschitz;
- 4) $l(\mathbf{x}_j, y_j; \mathbf{w}_s) = 0, \forall j \in s$, where \mathbf{w}_s is the weights of the trained model with samples s ;

then we have the following inequality,

$$\frac{1}{n} \sum_{i \in D} l(\mathbf{x}_i, y_i; \mathbf{w}_s) \leq \frac{\lambda^l(\lambda^f + 1)}{n} \sum_{j \in s} \sum_{i=1}^{k_j} \|\mathbf{x}_i - \mathbf{x}_j^c\| + 2\lambda^l \sum_{i \in D} |\epsilon_i|, \quad (5)$$

where k_j is the number of samples whose closest sample in s is \mathbf{x}_j^c ; $|\epsilon_i|$ is a sample from an independent random half-normal distribution with mean $\frac{\sigma\sqrt{2}}{\sqrt{\pi}}$ and variance $\sigma^2(1 - \frac{2}{\pi})$.

The left-hand side of the inequality is the average loss across the entire dataset. The right-hand side, i.e., the upper bound of the average loss, is correlated to the objective of a *K-Medoids Clustering* problem [36], where K is the number of labeled data samples for training ($K = |s|$). K-Medoids clustering problem is required to return K clusters from a set of points as well as K centers for each cluster. Therefore, minimizing $\sum_{j \in s} \sum_{i=1}^{k_j} \|\mathbf{x}_i - \mathbf{x}_j\|$ helps to bound the left-hand side.

Figure 13 provides an intuition for the K-Medoids clustering in a 2D space. Random selection may result in biased coverage of the entire dataset, causing significant overfitting of model training. K-Medoids clustering is able to select medoids (data) evenly from the space for training such that most unselected data samples are close to their nearest medoids.

Theorem III.3 requires both the loss function and the estimator to be Lipschitz continuous.

Lemma III.4. If the following conditions hold,

- 1) $\forall i \in D, (\mathbf{x}_i, y_i)$ satisfies $\|\mathbf{x}_i\| \leq b_1, |y_i| \leq b_2$;
- 2) $\hat{f}_{\mathbf{w}_s}(\mathbf{x})$ is $\lambda^{\hat{f}}$ -Lipschitz continuous w.r.t \mathbf{x} ;
- 3) $\exists (\mathbf{x}_0, y_0)$ such that $\hat{f}_{\mathbf{w}_s}(\mathbf{x}_0) = y_0 + \delta$, where δ is a bounded constant;

then square loss function $l_{\mathbf{w}_s}(\mathbf{x}, y) = (y - \hat{f}_{\mathbf{w}_s}(\mathbf{x}))^2$ is λ^l -Lipschitz continuous, where y is the label and $\hat{f}_{\mathbf{w}_s}(\cdot)$ is the learned function with parameter \mathbf{w}_s (also denoted as $\hat{f}(\cdot)$ for brevity),

$$\lambda^l = (4\lambda^{\hat{f}}b_1 + 4b_2 + 2|\delta|) \cdot \max(1, \lambda^{\hat{f}}). \quad (6)$$

In practice, the three assumptions are not difficult to hold. Consider the physical meaning of \mathbf{x} and y , both $\|\mathbf{x}\|$ and $|y|$ are numerically small in this work. Lemma III.5 proves that CNN/ResNet is Lipschitz continuous. If the training error for CNN/ResNet is small,

which is mostly true, (x_0, y_0) can be selected from the training dataset and then $|\delta|$ is also small.

Lemma III.5. A CNN/ResNet for regression with n_c convolution layers (with max-pooling and ReLU) and n_{fc} fully connected layers is $(1 + \alpha\sqrt{N})^{n_c+n_{fc}}$ -Lipschitz.

Detailed proofs for Theorem III.3, Lemma III.4, and Lemma III.5 can be found in Appendix.

IV. EXPERIMENTAL RESULTS

Our framework is implemented with Tensorflow [37] and validated on a Linux server with 3.4GHz Intel i7 CPU and Nvidia GTX 1080 GPU. The K-Medoids clustering is approximated by K-Means clustering in scikit-learn [38] and assigning the data points that are closest to centroids as medoids. We observe that this approach provides better and more stable objectives of K-Medoids clustering than does dedicated K-Medoids clustering solver in PyClust package in our experiments.

Around 980 mask clips are generated according to Section III-A for N10 and N7 separately following the design rules in Section II-B, respectively. N7_a and N7_b use the same set of clips, but different lithography configurations. SRAF, OPC and aerial image simulation are performed with Mentor Calibre [18]. The golden CD values are obtained from rigorous simulation using Synopsys Sentaurus Lithography models [39] calibrated from manufactured data for N10, N7_a, and N7_b according to Table I. Then golden thresholds are extracted. Each clip has four thresholds as shown in Figure 4. Hence the N10 dataset contains 3928 samples and each N7 dataset contains 3916 samples, respectively. The data augmentation technique in Section III-A2 is applied, so the training set and the testing set will be augmented by a factor of 8 independently. For example, if 50% of the data for N10 are used for training, then there are $3928 \times 50\% \times 8 = 15712$ samples. It needs to mention that always the same 50% portions are used during the validation of a dataset for fair comparison of different techniques. The batch size is set to 32 for training accommodating to the large variability in the sizes of training datasets. Adam [40] is used as the stochastic optimizer and maximum epoch is set to 200 for training.

The training time for one model takes 10 to 40 minutes according to the portions of a dataset used for training, and prediction time for an entire N10 or N7 dataset takes less than 10 seconds, while the rigorous simulation takes more than 15 hours for each N10 or N7 dataset. Thus we no longer report the prediction time which is negligible compared with that of the rigorous simulation. Each experiment runs 10 different random seeds and averages the numbers.

A. CNN and ResNet

We first compare CNN and ResNet in Figure 14(a). Column “CNN-5” denotes the network with 5 layers shown in Figure 11(a). Column “CNN-10” denotes the one with 10 layers that has the same structure as that in Figure 11(b) but without shortcut connections. Column “ResNet” denotes the one with 10 layers shown in Figure 11(b). When using 1% to 20% training data, ResNet shows better average relative RMS error ϵ_r^{th} than CNN-10, but CNN-5 provides the best error. We will show later that ResNet on the contrary outperforms CNN-5 when transfer learning is incorporated.

We then show the performance of active learning for CNN and ResNet in Figure 14(b) and Figure 14(c), denoted as “CNN-5+AL” and “ResNet+AL”, respectively. The beneficial amount of training data for active data selection is from 10% to 40%. For example, for 20% training data, it provides 11.6% accuracy improvement for

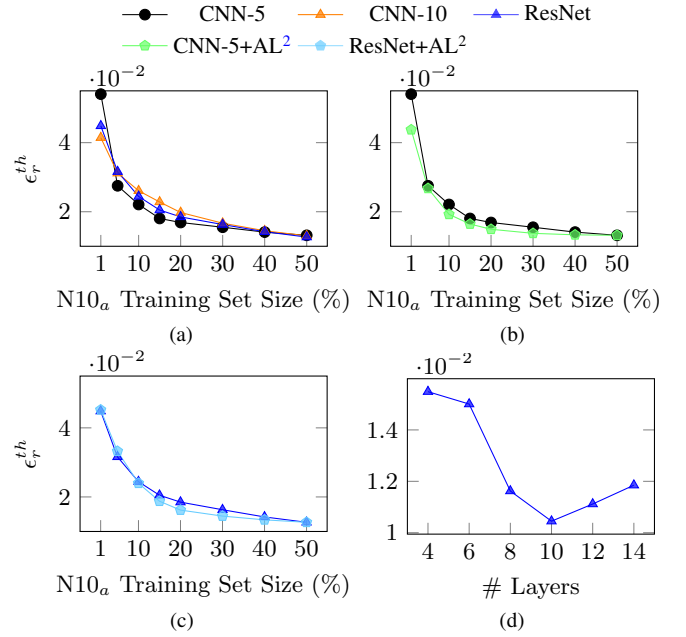


Fig. 14: (a) Comparison on testing accuracy of CNN-5, CNN-10, and ResNet on N10. (b) Testing accuracy of CNN with active learning on N10. (c) Testing accuracy of ResNet with active learning on N10. (d) Impact of depth on the testing accuracy of ResNet.

CNN and 12.5% for ResNet; for 30% training data, it provides 11.4% improvement for CNN and 11.3% for ResNet [41]. The benefit of active learning is not significant for extremely small training dataset, e.g., 1% and 5%. When there are very few training data, it is more likely for randomly selected data samples to distribute quite some distance away than to squeeze as small clusters. Although active selection of data can avoid corner cases of extremely poor sampling, e.g., all data samples squeezing as a small cluster, while it is difficult to demonstrate the benefit of active learning in ordinary cases. On the other hand, when the amount of training data increases, the benefit from active learning drops due to sufficient coverage. The rightmost points take all 50% training data and thus show the same accuracy as that without active learning.

The impacts of depth on the performance of ResNet are further explored in Figure 14(d), where we gradually stack more building blocks in Figure 10 before fully connected layers. The x-axis denotes total number of convolution and fully connected layers corresponding to different numbers of building blocks. For instance, 0 building block leads to 4 layers and 3 building blocks result in 10 layers (Figure 11(b)). The testing error decreases to lowest value at 10 layers and then starts to increase, indicating potential overfitting afterwards [32]. Therefore, we use 10 layers for the ResNet in the experiment.

B. Knowledge Transfer From N10 to N7

We then compare the testing accuracy between knowledge transfer from N10 to N7 and directly training from N7 datasets in Figure 15(a). In this example, the x-axis represents the percentage of training dataset for the target domain N7_a, while the percentage of data from the source domain N10 is always 50%. Similar trends are also observed for N7_b. Curve “CNN” denotes training the CNN of 5 layers in Figure 11(a) with data from target domain only, i.e., no

²Results for active learning extended from [41]

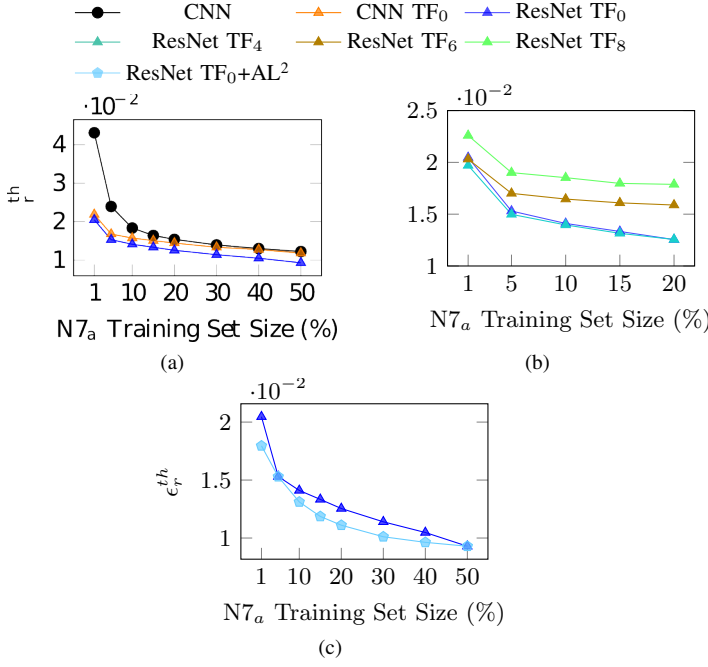


Fig. 15: Testing accuracy of transfer learning from N10 to N7_a. (a) Comparison between CNN and transfer learning. (b) Comparison between transfer learning schemes where different numbers of layers are fixed. (c) Comparison between transfer learning only and transfer learning plus active learning for ResNet.

transfer learning involved. Curve “CNN TF₀” denotes the transfer learning scheme in Section III-D for the same CNN with zero layer fixed. Curve “ResNet TF₀” denotes applying the same scheme to ResNet. The most significant benefit of transfer learning comes from small training dataset with a range of 1% to 20%, where there are around 52% to 18% improvement in the accuracy from CNN. Meanwhile, ResNet TF₀ can achieve an average of 13% smaller error than CNN TF₀.

Figure 15(b) further compares the results of fixing different numbers of layers during transfer learning. In this case, ResNet TF₀ and ResNet TF₄ have the best accuracy, while the error increases with more layers fixed. It is indicated that the tasks N10 and N7 are quite different and both feature extraction layers and regression layers need finetuning.

In Figure 15(c), we enable transfer learning plus active learning, which provides 7% to 11% additional accuracy improvement for 10% to 40% amount of training data from the target domain.

C. Knowledge Transfer within N7

The transfer learning between different N7 datasets, e.g., from N7_a to N7_b, is also explored in Figure 16. The x-axis represents the percentage of training dataset for the target domain N7_b, while the percentage of data from the source domain N7_a is always 50%. Compared with the knowledge transfer from N10 to N7, we achieve even higher accuracy between 1% and 20% training datasets in Figure 16(a). For example, with 1% training dataset, there is around 65% improvement in accuracy from CNN, and with 20% training dataset, the improvement is around 23%. ResNet TF₀ keeps having lower errors than that of CNN TF₀ as well, with an average benefit around 15%.

The curves in Figure 16(b) show different insights from that of the knowledge transfer from N10 to N7. The accuracy of ResNet

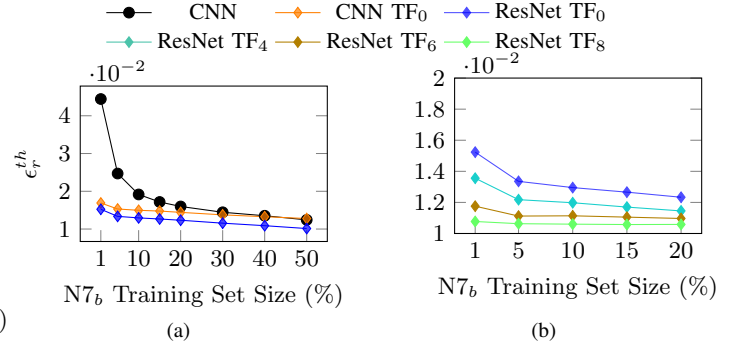


Fig. 16: Testing accuracy of transfer learning from N7_a to N7_b. (a) Comparison between CNN and transfer learning. (b) Comparison between transfer learning schemes where different numbers of layers are fixed.

TF₀ can be further improved with more layers fixed, e.g., ResNet TF₈, by around 28% to 14%. This is reasonable since N7_a and N7_b have the same design rules and illumination shapes, and the only difference lies in the resist materials. Therefore, the feature extraction layers are supposed to remain almost the same. With the sizes of the training dataset increasing to 15% and 20%, the differences in the accuracy become smaller, because there are enough data to find good configurations for the networks. Since knowledge transfer is remarkably effective with ResNet TF₈, we do not see the room for further improvement with active learning. Thus we did not plot the curves for that.

D. Impact of Various Source Domains

In transfer learning, the correlation between the datasets of source and target domains is critical to the effectiveness of knowledge transfer. Thus, we explore the impacts of source domain datasets on the accuracy of modeling for the target domain. Figure 17 plots the testing errors of learning N7_b using ResNet TF₀ with various source domain datasets. Curves “N10^{50%}” and “N7_a^{50%}” indicate that 50% of the N10 or the N7_a dataset is used to train source domain models, respectively. Curve “N10^{50%} + N7_a^{1%}” describes the situation where we have 50% of the N10 dataset and 1% of the N7_a dataset for training. In this case, as shown in Figure 18, we first use the 50% N10 data to train the first source domain model; then train the second source domain model using the first model as the starting point with the 1% N7_a data; in the end, the target domain model for N7_b is trained using the second model as the starting point with N7_b data. Curves “N10^{50%} + N7_a^{5%}” and “N10^{50%} + N7_a^{10%}” are similar, simply with different amounts of N7_a data for training.

The knowledge from N7_a^{50%} is the most effective for N7_b due to the minor difference in resist materials between two datasets. For the rest curves, the accuracy of N10^{50%} + N7_a^{5%} and N10^{50%} + N7_a^{10%} is in general better than or at least comparable to that of N10^{50%}. This indicates that having more data from closer datasets to the target dataset, e.g., N7_a, is still helpful.

E. Improvement in Data Efficiency

Table II presents the accuracy metrics, i.e., relative threshold RMS error (ϵ_r^{th}) and CD RMS error (ϵ^{CD}), for learning N7_b from various source domain datasets. Since we consider the data efficiency of different learning schemes, we focus on the small training dataset for N7_b, from 1% to 20%. Situations such as no source domain data (\emptyset), only source domain data from N10 (N10^{50%}), only source domain data from N7_a (N7_a^{50%}), and combined source domain datasets, are

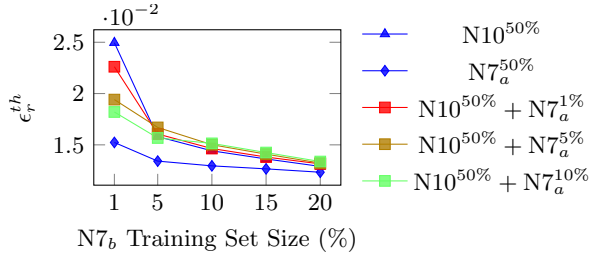


Fig. 17: Testing accuracy of ResNet TF₀ for N7_b from different source domain datasets.

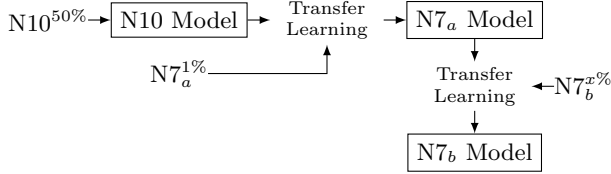


Fig. 18: Transfer learning from 50% of N10 dataset and 1% of N7_a dataset (i.e., $N10^{50\%} + N7_a^{1\%}$) to N7_b with $x\%$ of N7_b dataset.

examined. As mentioned in Section II, the fidelity between relative threshold RMS error and CD RMS error is very consistent, so they share almost the same trends. Transfer learning with any source domain dataset enables an average improvement of 23% to 40% from that without knowledge transfer. In small training datasets of N7_b, ResNet also achieves around 8% better performance on average than CNN in the transfer learning scheme. Enabling active learning together with transfer learning allows additional 5% accuracy improvement on average compared with transfer learning only for ResNet. At 1% of N7_b, combined source domain datasets have better performance compared with N10^{50%} only, but the benefits vanish with the increase of the N7_b dataset.

In real manufacturing, models are usually calibrated to satisfy a target accuracy or target CD RMS error. Figure 19 demonstrates the amount of training data required in the target domain for learning the N7_b model. Curve “CNN” does not involve any knowledge transfer, while curves “CNN TF₀” and “ResNet TF₀” utilize transfer learning in CNN and ResNet, respectively. The curves in Figure 19(a) assume the availability of N10 data. Consider the CD RMS error from 1.5nm to 2.5nm, which is around 10% of the half pitch for N7 contacts. This range of accuracy is also comparable to that of the state-of-the-art CNN [4]. ResNet TF₀ requires significantly fewer data than both CNN and CNN TF₀. For instance, when the target CD error is 1.75nm, ResNet TF₀ demands 5% training data from N7_b, while CNN requires 20% and CNN TF₀ requires 15%. By enabling active learning, ResNet TF₀+AL further reduces data requirement from ResNet TF₀, e.g., 1.5X and 4X fewer training data than ResNet TF₀ and CNN for 1.5nm, respectively. Figure 19(b) considers the transfer from N7_a to N7_b. Both ResNet TF₀ and CNN TF₀ only require 1% training data from N7_b for most target CD RMS errors, where CNN TF₀ cannot achieve the accuracy unless given 30% data. Overall, ResNet TF₀ can achieve 3-10X reduction of training data within this range compared with CNN. It needs to mention that 1% of dataset only correspond to fewer than 40 samples owing to the data augmentation, indicating only thresholds of 40 clips are required.

V. CONCLUSION

A transfer learning framework with a clustering based active data selection on residual neural networks is proposed for resist modeling. The combination of transfer learning and active learning

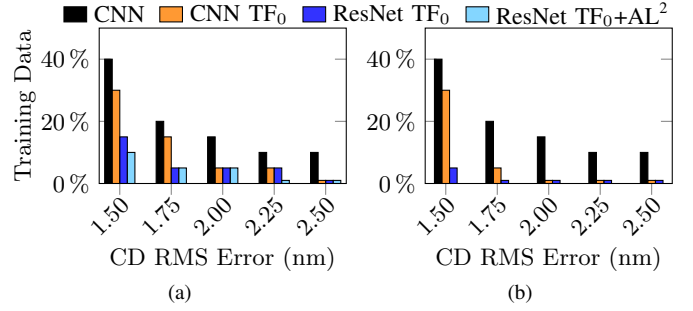


Fig. 19: Amount of training data required for N7_b given target CD RMS errors when (a) 50% N10 dataset is available or (b) 50% N7_a dataset is available.

for ResNet is able to achieve high accuracy with very few data from the target domain, under various situations for knowledge transfer, indicating high data efficiency. Extensive experiments demonstrate that the proposed techniques can achieve 3-10X reduction according to various requirements of accuracy comparable to the state-of-the-art learning approach. It is shown that the performance of transfer learning differs from dataset to dataset and is worth exploring to see the correlation between datasets. Active selection of data samples is also useful to guide the generation of mask designs for model calibration in manufacturing. Examining the quantitative relation between the correlation of datasets and performance of transfer learning is valuable in the future. There is still room to improve the effectiveness of knowledge transfer from N10 to N7 datasets. Therefore, in the future, we will actively explore other learning techniques to further improve the accuracy, such as preprocessing steps like scaling and normalization, various regularization techniques, and semi-supervised learning.

ACKNOWLEDGE

This project is supported in part by Toshiba Memory Corporation, NSF, and the University Graduate Continuing Fellowship from the University of Texas at Austin. The authors would like to thank Memory Lithography Group from Toshiba Memory Corporation and Dr. Kai Zhong from the Computer Science Department of UT Austin for helpful discussions and feedback.

REFERENCES

- [1] L. Liebmann, A. Chu, and P. Gutwin, “The daunting complexity of scaling to 7nm without EUV: Pushing DTCO to the extreme,” in *Proceedings of SPIE*, vol. 9427, 2015.
- [2] L. Liebmann, J. Zeng, X. Zhu, L. Yuan, G. Bouche, and J. Kye, “Overcoming scaling barriers through design technology cooptimization,” in *VLSI Technology, 2016 IEEE Symposium on*. IEEE, 2016, pp. 1–2.
- [3] S. Shim, S. Choi, and Y. Shin, “Machine learning-based resist 3d model,” in *Proc. of SPIE Vol.*, vol. 10147, pp. 101 471D–1.
- [4] Y. Watanabe, T. Kimura, T. Matsunawa, and S. Nojima, “Accurate lithography simulation model based on convolutional neural networks,” in *SPIE Advanced Lithography*. International Society for Optics and Photonics, 2017, pp. 101 470K–101 470K.
- [5] X. Ma, X. Zhao, Z. Wang, Y. Li, S. Zhao, and L. Zhang, “Fast lithography aerial image calculation method based on machine learning,” *Applied Optics*, vol. 56, no. 23, pp. 6485–6495, 2017.
- [6] J.-Y. Wu, F. G. Pikus, and M. Marek-Sadowska, “Efficient approach to early detection of lithographic hotspots using machine learning systems and pattern matching,” in *SPIE Advanced Lithography*. International Society for Optics and Photonics, 2011, pp. 79 740U–79 740U.
- [7] T. Matsunawa, S. Nojima, and T. Kotani, “Automatic layout feature extraction for lithography hotspot detection based on deep neural network,” in *Proceedings of SPIE*, 2016.

TABLE II: Relative Threshold RMS Error and CD RMS Error for N7_b with Different Source Domain Datasets

Source Datasets		\emptyset		N10 ^{50%}						N7 ^{50%} _a				N10 ^{50%} + N7 ^{5%} _a		N10 ^{50%} + N7 ^{10%} _a	
Neural Networks		CNN		CNN TF ₀		ResNet TF ₀		ResNet TF ₀ +AL ²		CNN TF ₀		ResNet TF ₀		ResNet TF ₀		ResNet TF ₀	
		ϵ_r^{th} (10 ⁻²)	ϵ^{CD}	ϵ_r^{th} (10 ⁻²)	ϵ^{CD}	ϵ_r^{th} (10 ⁻²)	ϵ^{CD}	ϵ_r^{th} (10 ⁻²)	ϵ^{CD}	ϵ_r^{th} (10 ⁻²)	ϵ^{CD}	ϵ_r^{th} (10 ⁻²)	ϵ^{CD}	ϵ_r^{th} (10 ⁻²)	ϵ^{CD}	ϵ_r^{th} (10 ⁻²)	ϵ^{CD}
N7 _b	1%	4.44	4.76	2.34	2.48	2.29	2.39	1.95	2.09	1.69	1.79	1.52	1.60	1.94	2.03	1.82	1.91
	5%	2.78	2.96	1.73	1.86	1.60	1.70	1.58	1.70	1.53	1.64	1.34	1.43	1.67	1.78	1.57	1.67
	10%	1.92	2.04	1.63	1.76	1.47	1.57	1.36	1.48	1.50	1.60	1.30	1.38	1.50	1.60	1.51	1.61
	15%	1.72	1.84	1.56	1.68	1.39	1.47	1.23	1.32	1.48	1.55	1.27	1.35	1.41	1.50	1.43	1.52
	20%	1.60	1.71	1.50	1.61	1.31	1.39	1.16	1.24	1.44	1.55	1.23	1.31	1.32	1.41	1.34	1.43
ratio		1.00	1.00	0.77	0.77	0.70	0.69	0.63	0.64	0.69	0.69	0.60	0.60	0.69	0.69	0.69	0.68

- [8] M. Shin and J.-H. Lee, "Accurate lithography hotspot detection using deep convolutional neural networks," in *Journal of Micro/Nanolithography, MEMS, and MOEMS (JM3)*, 2016.
- [9] H. Yang, J. Su, Y. Zou, B. Yu, and F. E. Young, "Layout hotspot detection with feature tensor generation and deep biased learning," in *ACM/IEEE Design Automation Conference (DAC)*, 2017.
- [10] H. Yang, Y. Lin, B. Yu, and F. E. Young, "Lithography hotspot detection: From shallow to deep learning," in *IEEE International System-on-Chip Conference (SOCC)*, 2017.
- [11] Y. Lin, X. Xu, J. Ou, and D. Z. Pan, "Machine learning for mask/wafer hotspot detection and mask synthesis," in *Photomask Technology*, vol. 10451. International Society for Optics and Photonics, 2017, p. 104510A.
- [12] A. Gu and A. Zakhori, "Optical proximity correction with linear regression," *IEEE Transactions on Semiconductor Manufacturing (TSM)*, vol. 21, no. 2, pp. 263–271, 2008.
- [13] N. Jia and E. Y. Lam, "Machine learning for inverse lithography: using stochastic gradient descent for robust photomask synthesis," *Journal of Optics*, vol. 12, no. 4, p. 045601, 2010.
- [14] R. Luo, "Optical proximity correction using a multilayer perceptron neural network," *Journal of Optics*, vol. 15, no. 7, p. 075708, 2013.
- [15] T. Matsunawa, B. Yu, and D. Z. Pan, "Optical proximity correction with hierarchical bayes model," *Journal of Micro/Nanolithography, MEMS, and MOEMS*, vol. 15, no. 2, pp. 021 009–021 009, 2016.
- [16] X. Xu, Y. Lin, M. Li, T. Matsunawa, S. Nojima, C. Kodama, T. Kotani, and D. Z. Pan, "Sub-Resolution Assist Feature Generation with Supervised Data Learning," *IEEE Transactions on Computer-Aided Design of Integrated Circuits and Systems (TCAD)*, vol. PP, no. 99, 2017.
- [17] C. B. Tan, K. K. Koh, D. Zhang, and Y. M. Foong, "Sub-resolution assist feature (sraf) printing prediction using logistic regression," in *Proceedings of SPIE*, 2015, pp. 94 261Y–94 261Y.
- [18] Mentor Graphics, "Calibre verification user's manual," 2008.
- [19] L. W. Liebmann, S. M. Mansfield, A. K. Wong, M. A. Lavin, W. C. Leipold, and T. G. Dunham, "Tcad development for lithography resolution enhancement," *IBM Journal of Research and Development*, vol. 45, no. 5, pp. 651–665, 2001.
- [20] J. P. Hanna and P. Stone, "Grounded action transformation for robot learning in simulation," in *AAAI*, 2017, pp. 3834–3840.
- [21] A. A. Rusu, N. C. Rabinowitz, G. Desjardins, H. Soyer, J. Kirkpatrick, K. Kavukcuoglu, R. Pascanu, and R. Hadsell, "Progressive neural networks," *arXiv preprint arXiv:1606.04671*, 2016.
- [22] S. J. Pan and Q. Yang, "A survey on transfer learning," *IEEE Transactions on knowledge and data engineering*, vol. 22, no. 10, pp. 1345–1359, 2010.
- [23] O. Sener and S. Savarese, "Active learning for convolutional neural networks: Acore-set approach," *stat*, vol. 1050, p. 27, 2017.
- [24] S. Tong and D. Koller, "Support vector machine active learning with applications to text classification," *Journal of machine learning research*, vol. 2, no. Nov, pp. 45–66, 2001.
- [25] C. Berland and R. Urner, "Active nearest neighbors in changing environments," in *International Conference on Machine Learning*, 2015, pp. 1870–1879.
- [26] J. Donahue, P. Krähenbühl, and T. Darrell, "Adversarial feature learning," *arXiv preprint arXiv:1605.09782*, 2016.
- [27] B. Demir and L. Bruzzone, "A multiple criteria active learning method for support vector regression," *Pattern recognition*, vol. 47, no. 7, pp. 2558–2567, 2014.
- [28] K. Fukumizu, "Statistical active learning in multilayer perceptrons," *IEEE Transactions on Neural Networks*, vol. 11, no. 1, pp. 17–26, 2000.
- [29] C. Zhuo, K. Agarwal, D. Blaauw, and D. Sylvester, "Active learning framework for post-silicon variation extraction and test cost reduction," in *Proceedings of the International Conference on Computer-Aided Design*. IEEE Press, 2010, pp. 508–515.
- [30] H. Lin and P. Li, "Classifying circuit performance using active-learning guided support vector machines," in *Proceedings of the International Conference on Computer-Aided Design*. ACM, 2012, pp. 187–194.
- [31] M. Li, K. Shamsi, T. Meade, Z. Zhao, B. Yu, Y. Jin, and D. Z. Pan, "Provably secure camouflaging strategy for ic protection," *IEEE Transactions on Computer-Aided Design of Integrated Circuits and Systems*, 2017.
- [32] I. Goodfellow, Y. Bengio, and A. Courville, *Deep learning*. MIT press, 2016.
- [33] K. He, X. Zhang, S. Ren, and J. Sun, "Deep residual learning for image recognition," in *Proceedings of the IEEE conference on computer vision and pattern recognition*, 2016, pp. 770–778.
- [34] Y. Bengio, P. Simard, and P. Frasconi, "Learning long-term dependencies with gradient descent is difficult," *IEEE transactions on neural networks*, vol. 5, no. 2, pp. 157–166, 1994.
- [35] X. Glorot and Y. Bengio, "Understanding the difficulty of training deep feedforward neural networks," in *Proceedings of the Thirteenth International Conference on Artificial Intelligence and Statistics*, 2010, pp. 249–256.
- [36] X. Jin and J. Han, *K-Medoids Clustering*. Boston, MA: Springer US, 2010, pp. 564–565. [Online]. Available: https://doi.org/10.1007/978-0-387-30164-8_426
- [37] M. Abadi, A. Agarwal, P. Barham, E. Brevdo, Z. Chen *et al.*, "TensorFlow: Large-scale machine learning on heterogeneous systems," 2015. [Online]. Available: <https://www.tensorflow.org>
- [38] F. Pedregosa, G. Varoquaux, A. Gramfort, V. Michel, B. Thirion, O. Grisel, M. Blondel, P. Prettenhofer, R. Weiss, V. Dubourg *et al.*, "Scikit-learn: Machine learning in Python," *Journal of Machine Learning Research*, vol. 12, pp. 2825–2830, 2011.
- [39] Synopsys, "Sentaurus Lithography," <https://www.synopsys.com/silicon/mask-synthesis/sentaurus-lithography.html>, 2016.
- [40] D. Kingma and J. Ba, "Adam: A method for stochastic optimization," *arXiv preprint arXiv:1412.6980*, 2014.
- [41] Y. Lin, Y. Watanabe, T. Kimura, T. Matsunawa, S. Nojima, M. Li, and D. Z. Pan, "Data efficient lithography modeling with residual neural networks and transfer learning," in *ACM International Symposium on Physical Design (ISPD)*, Monterey, CA, March 2018.

APPENDIX

Proof of Lemma III.5.

Proof. We assume the output after a series of convolution and fully connected layers is the prediction of the CNN for regression. Consider two inputs \mathbf{x} and \mathbf{x}' , with their representation $\mathbf{x}^{(d)}$ and $\mathbf{x}'^{(d)}$. We first show the Lipschitz property of convolution layers and fully connected layers. Any convolution or fully connected layer can be denoted as $\mathbf{x}_j^{(d)} = \sum_i w_{i,j}^{(d)} \mathbf{x}_i^{(d-1)}$. By assuming $\sum_i |w_{i,j}^{(d)}| \leq \alpha, \forall i, j, d$, we can state,

$$\|\mathbf{x}_j^{(d)} - \mathbf{x}'_j^{(d)}\| \leq \alpha \|\mathbf{x}^{(d-1)} - \mathbf{x}'^{(d-1)}\|. \quad (7)$$

Let $n^{(d)}$ be the dimension of $\mathbf{x}^{(d)}$, which is bounded by N ,

$$\begin{aligned} \|\mathbf{x}^{(d)} - \mathbf{x}'^{(d)}\| &= \sqrt{\sum_j \|\mathbf{x}_j^{(d)} - \mathbf{x}'_j^{(d)}\|^2}, \\ &\leq \sqrt{n^{(d)} \alpha^2 \|\mathbf{x}^{(d-1)} - \mathbf{x}'^{(d-1)}\|^2}, \\ &\leq \alpha \sqrt{n^{(d)}} \|\mathbf{x}^{(d-1)} - \mathbf{x}'^{(d-1)}\|, \\ &\leq \alpha \sqrt{N} \|\mathbf{x}^{(d-1)} - \mathbf{x}'^{(d-1)}\|. \end{aligned} \quad (8)$$

We then consider ReLU and max-pooling layers. For any ReLU layer, it is straightforward to verify the following inequality,

$$|\max(0, a) - \max(0, b)| \leq |a - b|. \quad (9)$$

Any max-pooling layer can be viewed as a convolution layer in which only one weight is 1 and others are 0. Thus, we can state for ReLU and max-pooling layers,

$$\|\mathbf{x}^{(d)} - \mathbf{x}'^{(d)}\| \leq \|\mathbf{x}^{(d-1)} - \mathbf{x}'^{(d-1)}\|. \quad (10)$$

Combining the Lipschitz property of all layers of CNN,

$$\|CNN(\mathbf{x}; \mathbf{w}) - CNN(\mathbf{x}'; \mathbf{w})\| \leq (\alpha \sqrt{N})^{n_c + n_{fc}} \|\mathbf{x} - \mathbf{x}'\|, \quad (11)$$

where \mathbf{w} is the weights for CNN.

For ResNet, a shortcut connection can be viewed as a layer d which takes input from layer $d-1$ and layer d' , i.e., $\mathbf{x}^{(d)} = \mathbf{x}^{(d-1)} + \mathbf{x}^{(d')}$, where $d-1 > d'$. Then we can state,

$$\begin{aligned} \|\mathbf{x}^{(d)} - \mathbf{x}'^{(d)}\| &= \|\mathbf{x}^{(d-1)} + \mathbf{x}^{(d')} - \mathbf{x}'^{(d-1)} - \mathbf{x}'^{(d')}\|, \\ &\leq \|\mathbf{x}^{(d-1)} - \mathbf{x}'^{(d-1)}\| + \|\mathbf{x}^{(d')} - \mathbf{x}'^{(d')}\|, \\ &\leq ((\alpha \sqrt{N})^{d-d'-1} + 1) \|\mathbf{x}^{(d')} - \mathbf{x}'^{(d')}\|, \\ &\leq (1 + \alpha \sqrt{N})^{d-d'-1} \|\mathbf{x}^{(d')} - \mathbf{x}'^{(d')}\|. \end{aligned} \quad (12)$$

Therefore, combining all layers of ResNet,

$$\|ResNet(\mathbf{x}; \mathbf{w}) - ResNet(\mathbf{x}'; \mathbf{w})\| \leq (1 + \alpha \sqrt{N})^{n_c + n_{fc}} \|\mathbf{x} - \mathbf{x}'\|. \quad (13)$$

We combine Eq. (11) and Eq. (13) for generalization to both CNN and ResNet.

□

Proof of Lemma III.4.

Proof. We first bound $|\hat{f}(\mathbf{x}_i)|$,

$$\begin{aligned} |\hat{f}(\mathbf{x}_i)| &\leq |\hat{f}(\mathbf{x}_0)| + |\hat{f}(\mathbf{x}_i) - \hat{f}(\mathbf{x}_0)|, \\ &\leq |y_0| + |\delta| + \lambda^{\hat{f}} \|\mathbf{x}_i - \mathbf{x}_0\|, \\ &\leq b_2 + |\delta| + \lambda^{\hat{f}} (\|\mathbf{x}_i\| + \|\mathbf{x}_0\|), \\ &\leq b_2 + |\delta| + 2\lambda^{\hat{f}} b_1. \end{aligned} \quad (14)$$

Then prove the Lipschitz-continuity of square loss function,

$$\begin{aligned} |l_{\mathbf{w}_s}(\mathbf{x}_i, y_i) - l_{\mathbf{w}_s}(\mathbf{x}_j, y_j)| &= |(y_i - \hat{f}(\mathbf{x}_i))^2 - (y_j - \hat{f}(\mathbf{x}_j))^2|, \\ &\leq |y_i - y_j - \hat{f}(\mathbf{x}_i) + \hat{f}(\mathbf{x}_j)| |y_i + y_j - \hat{f}(\mathbf{x}_i) - \hat{f}(\mathbf{x}_j)|, \\ &\leq (|y_i - y_j| + |\hat{f}(\mathbf{x}_i) - \hat{f}(\mathbf{x}_j)|) (|y_i| + |y_j| + |\hat{f}(\mathbf{x}_i)| + |\hat{f}(\mathbf{x}_j)|), \\ &\leq (|y_i - y_j| + \lambda^{\hat{f}} \|\mathbf{x}_i - \mathbf{x}_j\|) (4b_2 + 2|\delta| + 4\lambda^{\hat{f}} b_1), \\ &\leq (4\lambda^{\hat{f}} b_1 + 4b_2 + 2|\delta|) \cdot \max(1, \lambda^{\hat{f}}) (|y_i - y_j| + \|\mathbf{x}_i - \mathbf{x}_j\|). \end{aligned} \quad (15)$$

□

Proof of Theorem III.3.

Proof.

$$|l_{\mathbf{w}_s}(\mathbf{x}_i, y_i) - l_{\mathbf{w}_s}(\mathbf{x}_j, y_j)| \stackrel{(a)}{\leq} \lambda^l (|y_i - y_j| + \|\mathbf{x}_i - \mathbf{x}_j\|). \quad (16)$$

Inequality (a) uses the Lipschitz property of the loss function.

$$\begin{aligned} |y_i - y_j| &= |f(\mathbf{x}_i) + \epsilon_i - f(\mathbf{x}_j) - \epsilon_j|, \\ &\leq |f(\mathbf{x}_i) - f(\mathbf{x}_j)| + |\epsilon_i| + |\epsilon_j|, \\ &\stackrel{(b)}{\leq} \lambda^f \|\mathbf{x}_i - \mathbf{x}_j\| + |\epsilon_i| + |\epsilon_j|, \end{aligned} \quad (17)$$

Inequality (b) uses the Lipschitz property of the ground truth function f .

Combine previous two inequalities Eq. (16) and Eq. (17), we have,

$$\begin{aligned} |l_{\mathbf{w}_s}(\mathbf{x}_i, y_i) - l_{\mathbf{w}_s}(\mathbf{x}_j, y_j)| &\leq \lambda^l (\lambda^f \|\mathbf{x}_i - \mathbf{x}_j\| + |\epsilon_i| + |\epsilon_j| + \|\mathbf{x}_i - \mathbf{x}_j\|), \\ &= \lambda^l (\lambda^f + 1) \|\mathbf{x}_i - \mathbf{x}_j\| + \lambda^l (|\epsilon_i| + |\epsilon_j|). \end{aligned} \quad (18)$$

Denote the selected data samples as $(\mathbf{x}_j^c, y_j^c), \forall j \in \mathbf{s}$. Then assign each point i of the entire dataset to a cluster centered by its nearest selected data sample j , and suppose that there are k_j points within the cluster. Then the average loss of all data points is bounded as follows,

$$\begin{aligned} \frac{1}{n} \sum_{i \in D} l_{\mathbf{w}_s}(\mathbf{x}_i, y_i) &= \frac{1}{n} \sum_{j \in \mathbf{s}} \sum_{i=1}^{k_j} l_{\mathbf{w}_s}(\mathbf{x}_i, y_i), \\ &\stackrel{(c)}{\leq} \frac{1}{n} \sum_{j \in \mathbf{s}} \sum_{i=1}^{k_j} (l_{\mathbf{w}_s}(\mathbf{x}_j^c, y_j^c) + |l_{\mathbf{w}_s}(\mathbf{x}_i, y_i) - l_{\mathbf{w}_s}(\mathbf{x}_j^c, y_j^c)|), \\ &\stackrel{(d)}{\leq} \frac{1}{n} \sum_{j \in \mathbf{s}} \sum_{i=1}^{k_j} (0 + |l_{\mathbf{w}_s}(\mathbf{x}_i, y_i) - l_{\mathbf{w}_s}(\mathbf{x}_j^c, y_j^c)|), \\ &\stackrel{(e)}{\leq} \frac{1}{n} \sum_{j \in \mathbf{s}} \sum_{i=1}^{k_j} (\lambda^l (\lambda^f + 1) \|\mathbf{x}_i - \mathbf{x}_j^c\| + \lambda^l (|\epsilon_i| + |\epsilon_j^c|)), \\ &= \frac{\lambda^l (\lambda^f + 1)}{n} \sum_{j \in \mathbf{s}} \sum_{i=1}^{k_j} \|\mathbf{x}_i - \mathbf{x}_j^c\| + \frac{\lambda^l}{n} \sum_{j \in \mathbf{s}} \sum_{i=1}^{k_j} (|\epsilon_i| + |\epsilon_j^c|), \\ &= \frac{\lambda^l (\lambda^f + 1)}{n} \sum_{j \in \mathbf{s}} \sum_{i=1}^{k_j} \|\mathbf{x}_i - \mathbf{x}_j^c\| + \frac{\lambda^l}{n} \sum_{i \in D} |\epsilon_i| + \frac{\lambda^l}{n} \sum_{i \in \mathbf{s}} k_i |\epsilon_i^c|, \\ &= \frac{\lambda^l (\lambda^f + 1)}{n} \sum_{j \in \mathbf{s}} \sum_{i=1}^{k_j} \|\mathbf{x}_i - \mathbf{x}_j^c\| + \frac{\lambda^l}{n} \sum_{i \in D} \alpha_i |\epsilon_i|, \\ &\quad \text{where } \alpha_i = \begin{cases} 1, & i \in D \setminus \mathbf{s}, \\ k_i + 1, & i \in \mathbf{s}, \end{cases} \\ &\stackrel{(f)}{\leq} \frac{\lambda^l (\lambda^f + 1)}{n} \sum_{j \in \mathbf{s}} \sum_{i=1}^{k_j} \|\mathbf{x}_i - \mathbf{x}_j^c\| + \frac{\lambda^l}{n} \sum_{i \in D} \alpha_i \sum_{i \in D} |\epsilon_i|, \\ &\stackrel{(g)}{\leq} \frac{\lambda^l (\lambda^f + 1)}{n} \sum_{j \in \mathbf{s}} \sum_{i=1}^{k_j} \|\mathbf{x}_i - \mathbf{x}_j^c\| + 2\lambda^l \sum_{i \in D} |\epsilon_i|, \end{aligned} \quad (19)$$

Inequality (c) utilizes the fact that $a - b \leq \|a - b\|$. Inequality (d) uses the zero loss assumption. Inequality (e) embeds Eq. (18). We assume ϵ_i and ϵ_j^c follow the same normal distribution, because they come from the same dataset. Inequality (f) leverages the fact that $\sum_i a_i b_i \leq \sum_i a_i \sum_i b_i, \forall a_i, b_i \geq 0$. Inequality (g) cancels out n by $\sum_{i \in D} \alpha_i = 2n$, where $|\epsilon_i|$ is a sample from an independent random half-normal distribution with mean $\sigma \sqrt{\frac{2}{\pi}}$ and variance $\sigma^2(1 - \frac{2}{\pi})$.

□